

Calculation of Thermally-Induced Displacements in Spherically Domed Ion Engine Grids

George C. Soulas
Glenn Research Center, Cleveland, Ohio

The NASA STI Program Office . . . in Profile

Since its founding, NASA has been dedicated to the advancement of aeronautics and space science. The NASA Scientific and Technical Information (STI) Program Office plays a key part in helping NASA maintain this important role.

The NASA STI Program Office is operated by Langley Research Center, the Lead Center for NASA's scientific and technical information. The NASA STI Program Office provides access to the NASA STI Database, the largest collection of aeronautical and space science STI in the world. The Program Office is also NASA's institutional mechanism for disseminating the results of its research and development activities. These results are published by NASA in the NASA STI Report Series, which includes the following report types:

- **TECHNICAL PUBLICATION.** Reports of completed research or a major significant phase of research that present the results of NASA programs and include extensive data or theoretical analysis. Includes compilations of significant scientific and technical data and information deemed to be of continuing reference value. NASA's counterpart of peer-reviewed formal professional papers but has less stringent limitations on manuscript length and extent of graphic presentations.
- **TECHNICAL MEMORANDUM.** Scientific and technical findings that are preliminary or of specialized interest, e.g., quick release reports, working papers, and bibliographies that contain minimal annotation. Does not contain extensive analysis.
- **CONTRACTOR REPORT.** Scientific and technical findings by NASA-sponsored contractors and grantees.

- **CONFERENCE PUBLICATION.** Collected papers from scientific and technical conferences, symposia, seminars, or other meetings sponsored or cosponsored by NASA.
- **SPECIAL PUBLICATION.** Scientific, technical, or historical information from NASA programs, projects, and missions, often concerned with subjects having substantial public interest.
- **TECHNICAL TRANSLATION.** English-language translations of foreign scientific and technical material pertinent to NASA's mission.

Specialized services that complement the STI Program Office's diverse offerings include creating custom thesauri, building customized databases, organizing and publishing research results . . . even providing videos.

For more information about the NASA STI Program Office, see the following:

- Access the NASA STI Program Home Page at <http://www.sti.nasa.gov>
- E-mail your question via the Internet to help@sti.nasa.gov
- Fax your question to the NASA Access Help Desk at 301-621-0134
- Telephone the NASA Access Help Desk at 301-621-0390
- Write to:
NASA Access Help Desk
NASA Center for Aerospace Information
7121 Standard Drive
Hanover, MD 21076



Calculation of Thermally-Induced Displacements in Spherically Domed Ion Engine Grids

George C. Soulas
Glenn Research Center, Cleveland, Ohio

Prepared for the
29th International Electric Propulsion Conference
cosponsored by ERPS, Princeton University, NASA Glenn, NASA Jet Propulsion Laboratory,
Aerojet, EPPDYL, IEPC, Busek, and Mitsubishi Electric
Princeton, New Jersey, October 31–November 4, 2005

National Aeronautics and
Space Administration

Glenn Research Center

This report contains preliminary
findings, subject to revision as
analysis proceeds.

Available from

NASA Center for Aerospace Information
7121 Standard Drive
Hanover, MD 21076

National Technical Information Service
5285 Port Royal Road
Springfield, VA 22100

Available electronically at <http://gltrs.grc.nasa.gov>

Calculation of Thermally-Induced Displacements in Spherically Domed Ion Engine Grids

George C. Soulas
National Aeronautics and Space Administration
Glenn Research Center
Cleveland, Ohio 44135

Abstract

An analytical method for predicting the thermally-induced normal and tangential displacements of spherically domed ion optics grids under an axisymmetric thermal loading is presented. A fixed edge support that could be thermally expanded is used for this analysis. Equations for the displacements both normal and tangential to the surface of the spherical shell are derived. A simplified equation for the displacement at the center of the spherical dome is also derived. The effects of plate perforation on displacements and stresses are determined by modeling the perforated plate as an equivalent solid plate with modified, or effective, material properties. Analytical model results are compared to the results from a finite element model. For the solid shell, comparisons showed that the analytical model produces results that closely match the finite element model results. The simplified equation for the normal displacement of the spherical dome center is also found to accurately predict this displacement. For the perforated shells, the analytical solution and simplified equation produce accurate results for materials with low thermal expansion coefficients.

Nomenclature

a_n	Non-homogeneous solution variable
A_n	Non-homogeneous solution variable
A_{T0}, A_{T1}, A_{T2}	Constants for quadratic temperature equation
B_n	Non-homogeneous solution variable
C	Boundary condition constant
C_v	Displacement boundary condition constant
E	Elastic modulus
f	Homogeneous solution for displacement general solution
h	Shell thickness
h_{dome}	Spherical dome height
k	Defined variable
M_θ	Circumferential bending moment per unit length
M_ϕ	Meridional bending moment per unit length
n	Series summation variable
N	Defined variable
N_θ	Circumferential longitudinal force per unit length
N_ϕ	Meridional longitudinal force per unit length
P_n	Legendre function
$P_n^{(1)}$	Legendre, or spherical, function of the first kind
q	Shear function general solution
\bar{q}	Shear function non-homogeneous solution
$\bar{\bar{q}}$	Shear function homogeneous solution
Q_ϕ	Shear force per unit length
R	Spherical shell radius of curvature
r	Chord radial location
r_o	Spherical shell chord radius
T	Shell change in temperature distribution

v	Shell tangential displacement
w	Shell normal displacement
w_0	Displacement w at $\varphi = 0$
z	Radial direction in a spherical coordinate system
α	Thermal expansion coefficient
Δ	Non-homogeneous solution variable
Δr_0	Spherical shell change in chord radius
$\varepsilon_{\theta\theta}$	Circumferential strain
$\varepsilon_{\varphi\varphi}$	Meridional strain
$\varepsilon_{\theta\theta}^0$	Circumferential middle surface strain
$\varepsilon_{\varphi\varphi}^0$	Meridional middle surface strain
θ	Circumferential direction
κ_θ	Circumferential strain equation variable
κ_φ	Meridional strain equation variable
ν	Poisson's ratio
$\sigma_{\theta\theta}$	Circumferential (or hoop) stress
$\sigma_{\varphi z}$	Shear stress
$\sigma_{\varphi\varphi}$	Meridional stress
τ	Shell temperature distribution in meridional direction
τ_0	Shell temperature distribution through thickness
φ	Meridional direction
φ_e	Meridional spherical shell edge
χ	Displacement function general solution
$\bar{\chi}$	Displacement function non-homogeneous solution
$\bar{\bar{\chi}}$	Displacement function homogeneous solution
Ψ	Boundary condition constant

I. Introduction

A key ion engine component is the acceleration system, or ion optics assembly. The ion optics assembly is typically made up of two perforated electrodes, labeled the screen and accelerator grids. Critical dimensions that directly affect ion optics' performance and service life are the gap between the grids and the grid-to-grid aperture alignment.

During ion thruster operation, the grids are heated by power deposition from the plasma and conducted and radiated heat from other thruster surfaces. This heating typically results in a temperature distribution along the grid surface that is higher at the center of the beam extraction area and cooler at the beam extraction edge. To preclude buckling and control the thermal expansion of large area grids, the thruster grids are typically manufactured with a spherically domed shape. This shape significantly reduces compressive stresses that can cause buckling and causes both grids to thermally expand in the same direction to provide some control over the grid gap.

However, each grid is also differentially heated during ion thruster operation. The resulting uneven displacement of each grid during thruster operation causes the gap between the grids and the radial grid-to-grid aperture alignment to change from their preset values. Knowledge of the grid gap and aperture alignment during thruster operation is essential in properly assessing ion optics' performance and service life.

Direct measurements of grid gaps during thruster operation have been made, however, these measurements are difficult to do and consume considerable resources (refs. 1 to 5). The only known measurements of grid-to-grid aperture alignment during thruster operation are those of reference 3. Radial grid-to-grid aperture misalignment during thruster operation has typically been inferred by non-axisymmetric erosion of the accelerator apertures resulting from extended thruster operation. Accurately predicting the displacements of each grid both normal and tangential to the dome surface during thruster operation would be of value for predicting the grid gap and grid-to-grid aperture alignment, respectively. This is because grid gap and grid-to-grid aperture alignment changes at a particular location are merely the difference of the normal and tangential displacements, respectively, of each grid. Such a predictive technique would not only be of value for existing ion thruster designs, but also for future designs.

Predicting these displacements requires knowledge of two critical elements. The first element is the temperature distribution across each grid. The second element is the resulting, thermally-induced displacements of the grids from these temperature distributions. The latter element is the subject of this paper.

Predicting grid displacement during thruster operation from a given temperature distribution has been the topic of several past investigations, only a few of which are included in the reference section of this paper (refs. 6 to 8). All of these studies, however, relied on finite element structural analysis computer codes, or finite element models, to determine the thermally-induced displacements of the grids. While such a technique can be effective in accurately determining these displacements, it lends no direct insight as to how grid design parameters affect grid displacements. Although these models can be used indirectly in modeling experiments where design parameters can be varied to determine their impact on displacements, such an approach is inefficient due to the broad parameter space. A more useful predictive tool would be an analytical method.

This paper describes an analytical method for calculating the thermally-induced displacements of spherically domed grids. Displacements determined include those both normal and tangential to the grid surface for grid gap and grid-to-grid aperture alignment determinations, respectively. The theory of thin-walled spherical shells under thermal loads and the resulting stresses and moments are reviewed. The appropriate boundary conditions are applied for the determination of constants. Afterwards, normal and tangential displacements are derived. A simplified equation for the normal displacement at the center of the spherical dome is also derived. The process for including the effects of shell perforation is presented. Finally, the resulting analytical model is compared to the results from a finite element model.

II. Background—Thermal Stresses in a Thin-walled Spherical Shell

The theory of thin-walled shells of revolution under thermal loads varying both through the thickness and along surface was originally reported by Nowacki (ref. 9), and later by Johns (ref. 10). A summary of the theory and the analytical solutions for thermal stresses in thin-walled shells from reference 9 is presented below. It will serve as a background necessary for determining the thermally-induced displacements of a spherical dome and provide equations for determining thermally-induced stresses and moments. The notation used in reference 9 will be adopted here.

In the following analysis, only spherical shells of uniform thickness under an axisymmetric thermal loading (i.e., constant along the circumference) will be considered. It is assumed that the wall thickness is very small in comparison with the radius of curvature and that the normal stress through the wall thickness is zero, both of which are commonly assumed in thin shell theory (ref. 11). The change in curvature resulting from the thermally-induced displacements is assumed to be negligibly small and that buckling does not occur. Furthermore, it is assumed that all deformation is fully elastic and obeys Hooke's law. Finally, it is assumed that the material is homogeneous, so that material properties are isotropic.

Figure 1 defines the resultant forces and moments per unit length on an element of a spherical shell under an axisymmetric load. Because the shell thermal loading is assumed to be axisymmetric, the change in temperature is only a function of φ and z . The area of the element in figure 1 is, therefore, $R^2 \cdot d\varphi \cdot d\theta$. The radius of curvature, R , is to the middle surface. The resultant forces and moments per unit length are defined below as

$$\begin{aligned} N_{\varphi} &= \int_{-h/2}^{h/2} \sigma_{\varphi\varphi} \cdot dz & N_{\theta} &= \int_{-h/2}^{h/2} \sigma_{\theta\theta} \cdot dz & M_{\varphi} &= - \int_{-h/2}^{h/2} z \cdot \sigma_{\varphi\varphi} \cdot dz & M_{\theta} &= - \int_{-h/2}^{h/2} z \cdot \sigma_{\theta\theta} \cdot dz \\ Q_{\varphi} &= - \int_{-h/2}^{h/2} \sigma_{\varphi z} \cdot dz \end{aligned} \quad (1)$$

The equilibrium equations for this spherical shell element are given by

$$\frac{\partial}{\partial \varphi} [N_{\varphi} \cdot \sin(\varphi)] - N_{\theta} \cdot \cos(\varphi) - Q_{\varphi} \cdot \sin(\varphi) = 0 \quad (2)$$

$$\frac{\partial}{\partial \varphi} [Q_{\varphi} \cdot \sin(\varphi)] + N_{\varphi} \cdot \sin(\varphi) + N_{\theta} \cdot \sin(\varphi) = 0 \quad (3)$$

$$\frac{\partial}{\partial \varphi} [M_{\varphi} \cdot \sin(\varphi)] - M_{\theta} \cdot \cos(\varphi) - Q_{\varphi} \cdot R \cdot \sin(\varphi) = 0. \quad (4)$$

A more complete derivation of these equilibrium equations can be found in references 11 and 12.

As shown in figure 1, the displacement v is in the tangential direction of increasing φ and the displacement w is normal to the surface (i.e., it coincides with the z axis, or radial axis, in a spherical coordinate system). The deformations $\varepsilon_{\varphi\varphi}$ and $\varepsilon_{\theta\theta}$ are given by

$$\varepsilon_{\varphi\varphi} = \varepsilon_{\varphi\varphi}^0 + z \cdot \kappa_{\varphi} \quad \varepsilon_{\theta\theta} = \varepsilon_{\theta\theta}^0 + z \cdot \kappa_{\theta} \quad (5)$$

where

$$\varepsilon_{\varphi\varphi}^0 = \frac{1}{R} \cdot \left(\frac{dv}{d\varphi} + w \right) \quad \varepsilon_{\theta\theta}^0 = \frac{1}{R} \cdot [v \cdot \cot(\varphi) + w] \quad \kappa_{\varphi} = \frac{1}{R} \cdot \frac{d\chi}{d\varphi} \quad \kappa_{\theta} = \frac{\chi \cdot \cot(\varphi)}{R} \quad (6)$$

and

$$\chi = \frac{1}{R} \cdot \left(v - \frac{dw}{d\varphi} \right). \quad (7)$$

Here, $\varepsilon_{\varphi\varphi}^0$ and $\varepsilon_{\theta\theta}^0$ are the deformations of the spherical shell's middle surface.

The aforementioned deformations and stresses are related by Hooke's law. The deformations as a function of stresses $\sigma_{\varphi\varphi}$ and $\sigma_{\theta\theta}$ are given by

$$\varepsilon_{\varphi\varphi} = \frac{1}{E} \cdot (\sigma_{\varphi\varphi} - \nu \cdot \sigma_{\theta\theta}) + \alpha \cdot T \quad \varepsilon_{\theta\theta} = \frac{1}{E} \cdot (\sigma_{\theta\theta} - \nu \cdot \sigma_{\varphi\varphi}) + \alpha \cdot T. \quad (8)$$

Here, T is defined as the change in temperature and is a function of φ and z . To simplify this analysis, it will be assumed the change in temperature is linear with thickness so that

$$T(\varphi, z) = \tau_o(\varphi) + z \cdot \tau(\varphi). \quad (9)$$

Throughout the remainder of this paper, the change in temperature will be referred to as the temperature.

The deformation equations of eq. (8) can be solved for the stresses. These stresses can then be used to solve for the resultant forces and moments per unit length in eq. (1). Equation (7) can be recast with eqs. (5) and (6) to yield χ as a function of the middle surface deformations. By manipulating these equations further and introducing a new variable defined below

$$q = 4 \cdot Q_{\varphi} \cdot \frac{R}{h^2}, \quad (10)$$

the following two second order differential equations can be derived for a spherical shell of constant thickness under an axisymmetric thermal load

$$\frac{d^2 \chi}{d\varphi^2} + \cot(\varphi) \cdot \frac{d\chi}{d\varphi} - \cot^2(\varphi) \cdot \chi - \nu \cdot \chi + \frac{h^2 \cdot R}{4 \cdot N} = (1 + \nu) \cdot \alpha \cdot R \cdot \frac{d\tau}{d\varphi} \quad (11)$$

$$\frac{d^2 q}{d\varphi^2} + \cot(\varphi) \cdot \frac{dq}{d\varphi} - \cot^2(\varphi) \cdot q + \nu \cdot q - \frac{4 \cdot E \cdot R}{h} \cdot \chi = \frac{4 \cdot E \cdot R}{h} \cdot \alpha \cdot \frac{d\tau_o}{d\varphi}. \quad (12)$$

Here, N is defined as

$$N = \frac{E \cdot h^3}{12 \cdot (1 - \nu^2)} . \quad (13)$$

The general solutions for χ and q are the sum of their non-homogeneous and homogeneous solutions to the second order differential equations of eqs. (11) and (12)

$$\chi = \bar{\chi} + \bar{\bar{\chi}} \quad q = \bar{q} + \bar{\bar{q}} . \quad (14)$$

The non-homogeneous solutions will be solved first. To simplify the analysis, it will be assumed that the change in temperature through the thickness as a function of φ is constant. That is, although the temperature can vary through the thickness, the temperature variation as a function of thickness is the same everywhere on the spherical dome. As a result, $d\tau/d\varphi = 0$, so that the right hand side of eq. (11) is zero. To solve these differential equations, the first derivative of the function τ_o is expanded in a series with respect to the Legendre, or spherical, functions of the first kind, $P_n^{(1)}[\cos(\varphi)]$ (ref. 13), so that

$$\frac{d\tau_o}{d\varphi} = \sum_{n=1}^{\infty} a_n \cdot P_n^{(1)}[\cos(\varphi)] . \quad (15)$$

The non-homogeneous solutions for eqs. (11) and (12) are, therefore

$$\bar{\chi} = 2 \cdot \alpha \cdot \frac{R}{h} \cdot \sum_{n=1}^{\infty} A_n \cdot P_n^{(1)}[\cos(\varphi)] \quad (16)$$

$$\bar{q} = 2 \cdot \alpha \cdot \frac{R}{h} \cdot \sum_{n=1}^{\infty} B_n \cdot P_n^{(1)}[\cos(\varphi)] \quad (17)$$

where

$$A_n = -\frac{1+\nu}{\Delta} \left\{ 6 \cdot (1-\nu) \cdot \frac{R}{h} \cdot a_n \right\} \quad (18)$$

$$B_n = \frac{2 \cdot E}{\Delta} \left\{ [1-\nu-n \cdot (n+1)] \cdot a_n \right\} \quad (19)$$

$$\Delta = [1-n \cdot (n+1)]^2 - \nu^2 + 12 \cdot (1-\nu^2) \cdot \left(\frac{R}{h} \right)^2 \quad (20)$$

$$a_n = \frac{2 \cdot n+1}{2} \cdot \frac{(n-1)!}{(n+1)!} \cdot \int_0^\pi \frac{d\tau_o}{d\varphi} \cdot \sin(\varphi) \cdot P_n^{(1)}[\cos(\varphi)] \cdot d\varphi . \quad (21)$$

The homogeneous solutions of eqs. (11) and (12) are slowly convergent hypergeometric series (refs. 9, 11, and 12). For very thin shells where φ_e is not small, however, boundary loadings only affect stresses in the vicinity of the edge of the spherical dome (refs. 9 and 11). These stresses decrease rapidly toward the center of the shell. Therefore, it is possible to neglect χ and $d\chi/d\varphi$ when compared to $d^2\chi/d\varphi^2$ in eq. (11), and q and $dq/d\varphi$ when compared to $d^2q/d\varphi^2$ in eq. (12) (refs. 9, 11, and 12). With these assumptions, the homogeneous solutions to eqs. (11) and (12) for a closed spherical shell become

$$\bar{\bar{\chi}} = C \cdot e^{-k \cdot (\varphi_e - \varphi)} \cdot \cos[k \cdot (\varphi_e - \varphi) + \psi] \quad (22)$$

$$\bar{\bar{q}} = -\frac{4 \cdot N}{h^2 \cdot R} \cdot \frac{d^2 \bar{\bar{\chi}}}{d\varphi^2} = -\frac{8 \cdot N \cdot C \cdot k^2}{h^2 \cdot R} \cdot e^{-k \cdot (\varphi_e - \varphi)} \cdot \sin[k \cdot (\varphi_e - \varphi) + \psi] \quad (23)$$

where

$$k = \left[3 \cdot (1 - \nu^2) \cdot \left(\frac{R}{h} \right)^2 \right]^{1/4}. \quad (24)$$

The constants C and ψ are determined by applying an appropriate set of boundary conditions, which will be discussed later.

With the general solutions for q and χ above, the stresses per unit length can be solved. The solution for Q_φ is easily obtained from eq. (10). From the equilibrium eqs. (2) and (3), N_φ and N_θ can be solved with Q_φ

$$N_\varphi = -Q_\varphi \cdot \cot(\varphi) = -\frac{h^2}{4 \cdot R} \cdot q \cdot \cot(\varphi) \quad (25)$$

$$N_\theta = -\frac{dQ_\varphi}{d\varphi} = -\frac{h^2}{4 \cdot R} \cdot \frac{dq}{d\varphi} \quad (26)$$

Note that $dq/d\varphi$ is merely

$$\frac{dq}{d\varphi} = \frac{d\bar{q}}{d\varphi} + \frac{d\bar{\bar{q}}}{d\varphi} \quad (27)$$

where

$$\frac{d\bar{q}}{d\varphi} = 2 \cdot \alpha \cdot \frac{R}{h} \cdot \sum_{n=1}^{\infty} B_n \cdot \left\{ n \cdot (n+1) \cdot P_n[\cos(\varphi)] - \cot(\varphi) \cdot P_n^{(1)}[\cos(\varphi)] \right\} \quad (28)$$

and

$$\frac{d\bar{\bar{q}}}{d\varphi} = -\frac{8 \cdot N \cdot C \cdot k^3}{R \cdot h^2} \cdot e^{-k \cdot (\varphi_e - \varphi)} \cdot \left\{ \sin[k \cdot (\varphi_e - \varphi) + \psi] - \cos[k \cdot (\varphi_e - \varphi) + \psi] \right\}. \quad (29)$$

The moments are given by

$$M_\varphi = -N \cdot [\kappa_\varphi + \nu \cdot \kappa_\theta - (1 + \nu) \cdot \alpha \cdot \tau] = -\frac{N}{R} \cdot \left[\frac{d\chi}{d\varphi} + \nu \cdot \cot(\varphi) \cdot \chi - R \cdot (1 + \nu) \cdot \alpha \cdot \tau \right] \quad (30)$$

$$M_\theta = -N \cdot [\kappa_\theta + \nu \cdot \kappa_\varphi - (1 + \nu) \cdot \alpha \cdot \tau] = -\frac{N}{R} \cdot \left[\cot(\varphi) \cdot \chi + \nu \cdot \frac{d\chi}{d\varphi} - R \cdot (1 + \nu) \cdot \alpha \cdot \tau \right]. \quad (31)$$

Further note that $d\chi/d\varphi$ is merely

$$\frac{d\chi}{d\varphi} = \frac{d\bar{\chi}}{d\varphi} + \frac{d\bar{\bar{\chi}}}{d\varphi} \quad (32)$$

where

$$\frac{d\bar{\chi}}{d\varphi} = 2 \cdot \alpha \cdot \frac{R}{h} \cdot \sum_{n=1}^{\infty} A_n \cdot \left\{ n \cdot (n+1) \cdot P_n[\cos(\varphi)] - \cot(\varphi) \cdot P_n^{(1)}[\cos(\varphi)] \right\} \quad (33)$$

and

$$\frac{d\bar{\bar{\chi}}}{d\varphi} = C \cdot k \cdot e^{-k \cdot (\varphi_e - \varphi)} \cdot \left\{ \cos[k \cdot (\varphi_e - \varphi) + \psi] + \sin[k \cdot (\varphi_e - \varphi) + \psi] \right\}. \quad (34)$$

The average stresses $\sigma_{\varphi\varphi}$, $\sigma_{\theta\theta}$, and $\sigma_{\varphi z}$ given in eq. (1) are merely their respective forces per unit length divided by the thickness, h .

III. Analytical Model of Displacements of a Spherical Shell with an Expanding Fixed Edge

This section presents how the constants C and ψ for the above analysis are determined by applying an appropriate set of boundary conditions. Although Nowacki determined analytical solutions for the above stresses, he did not solve for the tangential and normal displacements (i.e., v and w , respectively). He did, however, provide a process for solving the displacements (ref. 9). The following presents this process and the resulting analytical solutions. Afterwards, a simplified analytical solution for the displacement at the center of the dome, w_o , is provided. Finally, the process for determining stresses and displacements using the analytical solutions of this study are presented.

A. Boundary Condition and Determination of Constants

The homogeneous equations for χ and q can now be solved for a specific set of boundary conditions. While these equations can be solved for any number of boundary conditions, a fixed (or clamped) edge support was used for this analysis. With a fixed edge support, spherical dome edge rotation and displacements in the direction of the chord radius at the edge of the spherical dome are prevented. To make the analysis results more applicable, it was further assumed that the edge support at r_o could be thermally expanded by Δr_o as shown in figure 2. During this expansion, the radius of curvature at the edge support also expands accordingly. Such an assumption is appropriate for spherically domed grids that have a fixed dome support that can expand from thermal heating. While such an assumption appropriately accounts for the thermal expansion of the grid mounting structure, this edge support is assumed to be infinitely rigid, which is not typically the case with a true ion optics mounting system. Unfortunately, mounting system designs vary, and the specific mounting system design will affect the boundary conditions that should be used in this analysis. The results of this analysis will, therefore, be specific to the selected boundary conditions above. However, the following analysis can easily be repeated for a new set of boundary conditions.

Regarding the temperature, a further assumption made here is that the temperature is constant throughout the thickness of the grid. Given that most grid thicknesses are small relative to the radius of curvature and that the material is perforated, the assumption is reasonable. So, the temperature distribution is given by

$$T(\varphi, z) \approx T(\varphi) = \tau_o(\varphi). \quad (35)$$

It will be shown that the boundary conditions for thermally expanding fixed edge support are $\chi(\varphi_e) = 0$ and $\epsilon_{\theta\theta}(\varphi_e) = \Delta r_o / r_o$. With the above boundary condition, the constants C and ψ in the homogeneous solutions of eqs. (22) and (23) can be determined. At $\varphi = \varphi_e$, it can be shown that

$$v(\varphi_e) = \Delta r_o \cdot \cos(\varphi_e) \quad (36)$$

$$w(\varphi_e) = \Delta r_o \cdot \sin(\varphi_e) \quad (37)$$

$$\frac{dw(\varphi_e)}{d\varphi} = \Delta r_o \cdot \cos(\varphi_e) \quad (38)$$

Using the results of eqs. (36) and (38) in eq. (7), it is found that $\chi(\varphi_e) = 0$. When the non-homogeneous and homogeneous solutions of eqs. (16) and (22), respectively, are used to solve χ at $\varphi = \varphi_e$, the constant C is found to be

$$C = -\frac{\bar{\chi}(\varphi_e)}{\cos(\psi)}. \quad (39)$$

Because the edge support can expand by Δr_o , the strain at the edge support is, by definition, $\varepsilon_{\theta\theta}(\varphi_e) = \Delta r_o/r_o$. Equations (1), (25), and (26) can be used in eq. (8) of $\varepsilon_{\theta\theta}$ to yield

$$\frac{\Delta r_o}{r_o} = \varepsilon_{\theta\theta}(\varphi_e) = \frac{1}{E} \cdot \left(\frac{N_\theta}{h} - \nu \cdot \frac{N_\varphi}{h} \right) + \alpha \cdot \tau_o = -\frac{h}{E \cdot 4 \cdot R} \cdot \left(\frac{dq}{d\varphi} - q \cdot \nu \cdot \cot(\varphi) \right) + \alpha \cdot \tau_o. \quad (40)$$

The non-homogeneous and homogeneous solutions of eqs. (17) and (23), respectively, are used to solve for q and this, along with eq. (36) for $v(\varphi_e)$, can be used in eq. (40) above. The constant ψ is, thus, found to be

$$\psi = \arctan \left\{ \frac{R^2 \cdot \left[-\frac{h^2}{4 \cdot R} \cdot \left(\frac{d\bar{q}(\varphi_e)}{d\varphi} - \bar{q}(\varphi_e) \cdot \nu \cdot \cot(\varphi_e) \right) + h \cdot E \cdot \left(\alpha \cdot \tau_o(\varphi_e) - \frac{\Delta r_o}{r_o} \right) \right] + 2 \cdot N \cdot k^3 \cdot \bar{\chi}(\varphi_e)}{2 \cdot N \cdot k^2 \cdot [k - \nu \cdot \cot(\varphi_e)] \cdot \bar{\chi}(\varphi_e)} \right\}. \quad (41)$$

Note that the constants C and ψ above are for a fixed edge support that can expand by Δr_o . To obtain a solution for a fixed edge with no expansion, the edge expansion term Δr_o is merely set to zero.

B. Derivation of Tangential and Normal Displacements

With the aforementioned equations for forces per unit length solved, the displacement of the spherical dome in the v and w directions, shown in figure 1, can now be solved. The middle surface strain equations for $\varepsilon_{\varphi\varphi}^0$ and $\varepsilon_{\theta\theta}^0$ of eq. (6) can be combined to yield

$$\frac{dv}{d\varphi} - \nu \cdot \cot(\varphi) = R \cdot (\varepsilon_{\varphi\varphi}^0 - \varepsilon_{\theta\theta}^0). \quad (42)$$

The strain equations $\varepsilon_{\varphi\varphi}$ and $\varepsilon_{\theta\theta}$ of eq. (8) can be recast to give the stresses $\sigma_{\varphi\varphi}$ and $\sigma_{\theta\theta}$ as a function of the strains $\varepsilon_{\varphi\varphi}$ and $\varepsilon_{\theta\theta}$. These stresses can be integrated in the first two integrals of eq. (1) to yield N_φ and N_θ as a function of the middle surface strains $\varepsilon_{\varphi\varphi}^0$ and $\varepsilon_{\theta\theta}^0$ (ref. 9)

$$N_\varphi = \frac{E \cdot h}{1 - \nu^2} \cdot \left[\varepsilon_{\varphi\varphi}^0 + \nu \cdot \varepsilon_{\theta\theta}^0 - (1 + \nu) \cdot \alpha \cdot \tau_o \right] \quad (43)$$

$$N_\theta = \frac{E \cdot h}{1 - \nu^2} \cdot \left[\varepsilon_{\theta\theta}^0 + \nu \cdot \varepsilon_{\varphi\varphi}^0 - (1 + \nu) \cdot \alpha \cdot \tau_o \right]. \quad (44)$$

Equations (43) and (44) above can be recast to give $\varepsilon_{\varphi\varphi}^0$ and $\varepsilon_{\theta\theta}^0$ as functions of N_φ and N_θ . These can then be used in eq. (42), along with eqs. (25) and (26) for N_φ and N_θ , respectively, to yield

$$\frac{dv}{d\varphi} - v \cdot \cot(\varphi) = \frac{R \cdot (1 + \nu)}{E \cdot h} \cdot (N_\varphi - N_\theta) = \frac{(1 + \nu) \cdot h}{4 \cdot E} \left[\frac{dq}{d\varphi} - q \cdot \cot(\varphi) \right]. \quad (45)$$

The differential equation above can be solved by assuming a general solution

$$v(\varphi) = \frac{(1 + \nu) \cdot h}{4 \cdot E} \cdot q(\varphi) + f(\varphi) \quad (46)$$

where $f(\varphi)$ represents the homogeneous solution portion of the general solution. The general solution above can be used in eq. (42) to yield

$$\frac{df}{d\varphi} - f \cdot \cot(\varphi) = 0 \quad (47)$$

whose solution is

$$f(\varphi) = C_v \cdot \sin(\varphi). \quad (48)$$

The general solution for v is, therefore

$$v = \frac{(1 + \nu) \cdot h}{4 \cdot E} \cdot q + C_v \cdot \sin(\varphi). \quad (49)$$

The solution for the displacement w can be found substituting eq. (49) for v back into the middle surface strain equation for $\varepsilon_{\theta\theta}^0$ of eq. (6). Using the equation for $\varepsilon_{\theta\theta}^0$ as a function of N_φ and N_θ , along with eqs. (25) and (26) for N_φ and N_θ , respectively, it can be shown that

$$w = R \cdot \alpha \cdot \tau_o - \frac{h}{4 \cdot E} \cdot \left[\frac{dq}{d\varphi} + q \cdot \cot(\varphi) \right] - C_v \cdot \cos(\varphi). \quad (50)$$

The constant C_v can be determined by noting that at $\varphi = \varphi_e$, v is given by equation (36). It can be shown that

$$C_v = \frac{\Delta r_o \cdot \cos(\varphi_e) - \frac{(1 + \nu) \cdot h}{4 \cdot E} \cdot q(\varphi_e)}{\sin(\varphi_e)}. \quad (51)$$

C. Simplified Analytical Expression for the Displacement w_o at the Spherical Dome Center

The displacement w at the center of the spherical dome, or $\varphi = 0$, is of interest because this location experiences the largest displacement for a temperature distribution that monotonically decreases with increasing φ . The displacement can be simplified by noting that as φ approaches zero, q in equation (50) for w goes to zero. This is because the non-homogeneous solution of q in eq. (17) is zero since $P_n^{(1)}(1) = 0$ and the homogeneous solution of q in eq. (23) is negligibly small because it is multiplied by $\exp(-k\varphi_e)$, which is a small value for large ratios of radius of curvature to thickness. Furthermore, it can be shown that $dq/d\varphi$ also becomes negligibly small as φ approaches zero. This is because the homogeneous solution of $dq/d\varphi$ in eq. (29) is also negligibly small since it is also multiplied by $\exp(-k\varphi_e)$ and the non-homogeneous solution of $dq/d\varphi$ in eq. (28) typically produces a negligibly small value near the center.

These findings are not too surprising. The terms q and $dq/d\varphi$ are directly proportional to $\sigma_{\varphi\varphi}$ and $\sigma_{\theta\theta}$, respectively. One benefit of spherically-domed shells under thermal loads is that these stresses tend to decrease significantly near the center of the dome, as opposed to flat plates, whose stresses tend to increase under similar thermal loads. This is because the spherical domes have a preferential direction in which to thermally expand.

So, the resulting displacement w at $\varphi = 0$ reduces to

$$w_o \approx R \cdot \alpha \cdot T(0) - C_v. \quad (52)$$

The first term on the right hand side of the above equation represents the thermal expansion of a spherical shell of radius R , thermal expansion coefficient α , and temperature T at $\varphi = 0$. The second term (i.e., C_v) represents the effect of the boundary condition, given in eq. (51).

The expression for C_v is complicated because it includes $q(\varphi_e)$. It is, however, possible to simplify this expression. The homogeneous solution to q is given by combining eqs. (23) and (39) at $\varphi = \varphi_e$ to give

$$\bar{\bar{q}}(\varphi_e) = \frac{8 \cdot N \cdot k^2}{h^2 \cdot R} \cdot \tan(\psi) \cdot \bar{\chi}(\varphi_e) \quad (53)$$

Using this, along with eq. (41) for ψ , the general solution to $q(\varphi_e)$ becomes

$$q(\varphi_e) = \bar{q}(\varphi_e) + \frac{-\left(\frac{d\bar{q}(\varphi_e)}{d\varphi} - \bar{q}(\varphi_e) \cdot v \cdot \cot(\varphi_e)\right) + \frac{4 \cdot R \cdot E}{h} \cdot \left(\alpha \cdot \tau_o(\varphi_e) - \frac{\Delta r_o}{r_o}\right) + \frac{8 \cdot N \cdot k^3}{R \cdot h^2} \cdot \bar{\chi}(\varphi_e)}{k - v \cdot \cot(\varphi_e)}. \quad (54)$$

Using eqs. (16), (17), and (28) in the above equation, it can be shown that

$$q(\varphi_e) = \frac{\frac{4 \cdot R \cdot E}{h} \cdot \left(\alpha \cdot \tau_o(\varphi_e) - \frac{\Delta r_o}{r_o}\right)}{k - v \cdot \cot(\varphi_e)} + \frac{2 \cdot \alpha \cdot \frac{R}{h} \cdot \sum_{n=1}^{\infty} \left\{ B_n \cdot \left[(k + \cot(\varphi_e)) \cdot P_n^{(1)}[\cos(\varphi_e)] - n \cdot (n+1) \cdot P_n[\cos(\varphi_e)] \right] + \frac{2 \cdot E \cdot k}{\sqrt{3 \cdot (1-v^2)}} \cdot A_n \cdot P_n^{(1)}[\cos(\varphi_e)] \right\}}{k - v \cdot \cot(\varphi_e)} \quad (55)$$

For thin shells, R/h is large when compared to n^2 in the series summation, so eq. (20) for Δ reduces to

$$\Delta \approx 12 \cdot (1-v^2) \cdot \left(\frac{R}{h}\right)^2 \quad (56)$$

so that eqs. (18) and (19) for A_n and B_n , respectively, reduce to

$$A_n \approx -\frac{h}{2 \cdot R} \cdot a_n \quad (57)$$

$$B_n \approx \frac{[1 - v - n \cdot (n+1)] \cdot E \cdot a_n}{6 \cdot (1-v^2) \cdot \left(\frac{R}{h}\right)^2} \quad (58)$$

These equations can now be used in eq. (55). It can be shown that the first term in the series summation of eq. (55) is always negligibly small compared to the second term. Equation (55), therefore, reduces to

$$q(\varphi_e) \approx \frac{\frac{4 \cdot R \cdot E}{h} \cdot \left(\alpha \cdot \tau_o(\varphi_e) - \frac{\Delta r_o}{r_o}\right) - \frac{2 \cdot \alpha \cdot E \cdot k}{\sqrt{3 \cdot (1-v^2)}} \cdot \sum_{n=1}^{\infty} a_n \cdot P_n^{(1)}[\cos(\varphi_e)]}{k - v \cdot \cot(\varphi_e)}. \quad (59)$$

But the series summation of the above equation is merely the temperature gradient of eq. (15). Using this with the temperature assumption of eq. (35) in the above equation yields

$$q(\varphi_e) \approx \frac{\frac{4 \cdot R \cdot E}{h} \cdot \left(\alpha \cdot T(\varphi_e) - \frac{\Delta r_o}{r_o} \right) - \frac{2 \cdot \alpha \cdot E \cdot k}{\sqrt{3 \cdot (1 - \nu^2)}} \cdot \frac{dT(\varphi_e)}{d\varphi}}{k - \nu \cdot \cot(\varphi_e)}. \quad (60)$$

With this simplified expression for q at $\varphi = \varphi_e$, eq. (60) can be used in eq. (51) for C_v to yield

$$C_v \approx \Delta r_o \cdot \cot(\varphi_e) - \frac{(1 + \nu) \cdot \left\{ R \cdot \left(\alpha \cdot T(\varphi_e) - \frac{\Delta r_o}{r_o} \right) - \frac{\alpha \cdot k \cdot h}{\sqrt{12 \cdot (1 - \nu^2)}} \cdot \frac{dT(\varphi_e)}{d\varphi} \right\}}{k \cdot \sin(\varphi_e) - \nu \cdot \cos(\varphi_e)}. \quad (61)$$

Equations (52) and (61) define a simplified expression for the displacement of the center of the spherical dome requiring knowledge of material properties, geometry of the dome, temperatures at the center and edge, and the derivative of the temperature at the edge. As expected, the deflection of the dome center is a function of the material's Poisson's ratio but is independent the material elastic modulus.

D. Solution Process for Thermally-Induced Moments, Stresses, and Displacements

The process for solving for the thermally-induced displacements of the spherically domed shell, along with the stresses and moments, is presented below. The required inputs include shell material properties, geometry, and temperature distribution. Shell material properties include α , ν , and E . Shell geometry inputs include R , h , and φ_e . Often, however, only the dome height and chord radius are known. The radius of curvature can then be determined by

$$R = \frac{r_o^2 + h_{\text{dome}}^2}{2 \cdot h_{\text{dome}}} \quad (62)$$

while φ_e is determined by

$$\varphi_e = \arcsin\left(\frac{r_o}{R}\right). \quad (63)$$

The temperature distribution must be some continuous mathematical function of φ . Finally, a value for Δr_o is required.

The derivative of the temperature distribution, $dT/d\varphi = d\tau_o/d\varphi$, is first determined. This result is used in eq. (21) to determine the values for a_n . Solutions to the spherical functions of the first kind, along with the Legendre functions, can be defined using known Legendre explicit expressions and recurrence relations for higher orders and degrees (ref. 13). The results for a_n , along with Δ from eq. (20), are used in eqs. (18) and (19) to determine values for A_n and B_n , respectively. These results are then used in eqs. (16), (17), (33), and (28) to determine the non-homogeneous solutions of χ , q , $d\chi/d\varphi$, and $dq/d\varphi$, respectively. The results of these four equations are used with the temperature at $\varphi = \varphi_e$ to determine the constants ψ and C of eqs. (41) and (39), respectively. With these constants and eqs. (24) and (13) for k and N , respectively, the homogenous solutions to χ , q , $d\chi/d\varphi$, and $dq/d\varphi$, in eqs. (22), (23), (34), and (29), respectively, can be determined. The general solutions of χ , q , $d\chi/d\varphi$, and $dq/d\varphi$ are, therefore, the sum of their respective non-homogeneous and homogeneous solutions. With these solutions, Q_φ , N_θ and N_φ are determined with eqs. (10), (25), and (26), respectively. The moments M_φ and M_θ are determined with eqs. (30) and (31). The average stresses $\sigma_{\varphi\varphi}$, $\sigma_{\theta\theta}$, and $\sigma_{\varphi z}$ are merely the forces per unit length divided by the thickness, h .

Regarding displacements, the constant C_v in eq. (51) is determined with the general solution of q . With this result and the general solution for q , the tangential displacement, v , is solved with eq. (49). The general solutions of q and $dq/d\varphi$ are used to determine the normal displacement, w , in eq. (50).

There are limitations to the solutions to N_θ , N_ϕ , M_ϕ , M_θ , and w . Specifically, the solutions to these equations produce a singularity at $\phi = 0$, which is the geometric center of the spherical dome. This is due to the $\cot(\phi)$ term in each equation. That the $\cot(\phi)$ term was not properly accounted for in the solutions is an artifact of the assumption made for the homogeneous solutions of χ and q . However, solutions can be obtained in the immediate vicinity of $\phi = 0$ and the results extrapolated to the dome center.

The non-homogeneous solutions of χ and q in eqs. (16) and (17), respectively, and their derivatives include a series summation to infinity. These summations converge after some number of summations, so that some limiting value other than infinity can be used. To determine this value, it is important to understand that the non-homogeneous solutions to the differential equations of eqs. (11) and (12) were found by assuming that the derivative of the temperature distribution across the spherical dome could be expressed by the series summation in eq. (15). The required number of summations is, therefore, the number of summations necessary for eq. (15) to accurately express the actual derivative of the temperature as a function of ϕ . For larger values of n , a_n becomes negligibly small to ensure a convergent solution. So the required number of summations can be determined by comparing the actual derivative of the temperature distribution with that of eq. (15).

IV. Effects of Shell Perforation

Because ion optics are perforated, the effect of this perforation on the displacements must be included in the analytical model. Fortunately, determining the stresses and strains of perforated plates has been dealt with considerably in literature, examples of which are included in references 6, 14 to 17. The effects of plate perforation on displacements and stresses are determined by modeling the perforated plate as an equivalent solid plate with modified, or effective, material properties. The effective material properties include the elastic modulus and the Poisson's ratio (ref. 15). The resulting effective material properties are functions of the perforation pattern layout, aperture center-to-center spacing, and aperture diameter (ref. 14). With these effective material properties, displacements and nominal stresses are determined. The displacements in the actual perforated plate are the same as those of the equivalent solid plate utilizing effective material properties. Actual ligament stresses are determined by multiplying the nominal stresses with predetermined stress multipliers (ref. 14).

While this process offers significant simplicity, a short-coming is that effective material properties can be a function of the type of load applied to the perforated plate. This is especially true for thinner plates with a high perforated open area fraction and where the ratio of the material thickness divided by the center-to-center aperture spacing is small (ref. 15). The resulting equivalent solid plate possesses effective material properties that are not isotropic, which violates a basic assumption used in developing theory of thermal displacements in thin-walled shells. A thermally-loaded spherically domed grid will have both in plane stresses (i.e., thermally-induced compressive and tensile loads in the plane of the perforation), and bending loads. Therefore, if effective elastic moduli and Poisson's ratios vary with the type of load, this will introduce errors in determining displacements.

Effective material properties that account for perforation can be determined theoretically (refs. 14 to 17) or via finite element modeling (ref. 6). The latter technique is labor-intensive and can be shown to produce results that are similar to those of the theoretical study of reference 14. The theoretical studies of references 14 to 17 demonstrated that the ratios of effective to actual E and ν are functions of the minimum webbing width divided by the center-to-center aperture spacing for a given aperture layout. These studies also provided plots so that effective material properties could be readily determined for a given ratio of minimum webbing width to center-to-center aperture spacing.

V. Comparison of Analytical Model with Finite Element Model Results

The analytical model above was compared to the results from the finite element model in reference 6 by Shunk. Comparisons were made to both solid and perforated spherical shells with varying geometric and material properties. This was done so that the efficacy of the analytical solution and the process for accounting for perforation could be investigated separately over a relatively broad range of material and geometric properties. Furthermore, comparisons were only made for displacements normal to the surface because only these data were available for comparisons. Regardless, some tangential displacements from the analytical model will be presented.

Determining the efficacy of this analytical model by comparing it to a finite element model was done for three reasons. First, comparisons were direct because inputs such as boundary conditions and temperature distributions could be exactly matched (i.e., both used fixed edge supports). Second, comparisons could be made throughout the spherical dome because these data could be easily determined from the finite element model. Finally, measured data

with similar boundary conditions and free of other factors that could obfuscate comparisons could not be found by this author.

A. Solid Shell Normal Displacements

The finite element model in reference 6 was used to calculate the thermally-induced displacements normal to the spherical surface, w , as a function of chord radius for three different materials (i.e., 304 stainless steel, titanium, and molybdenum) and for two different chord radii (i.e., 50 and 75 cm). Although the aforementioned analytical model yields results as a function of ϕ , this variable can be converted to a chord radial dimension with the following relation

$$r = R \cdot \sin(\phi) . \quad (64)$$

For this comparison, the spherical domes were assumed to be solid, and not perforated. Material properties are listed in table 1. The screen grid thicknesses of table 2 were used. Geometric properties of the screen grid spherical domes listed in table 3 were used. The temperature distribution used here was that developed in reference 6. The temperature as a function of chord radius was a second order quadratic expression

$$T(\phi) = A_{T0} + A_{T1} \cdot R \cdot \sin(\phi) + A_{T2} \cdot R^2 \cdot \sin^2(\phi) . \quad (65)$$

The constants used in the above temperature equation are those for the screen grids listed in table 4. Finally, the boundary condition in reference 6 was a clamped edge with no chord expansion, so that Δr_o was equal to zero in the analytical model.

The normal displacements from the analytical and finite element models are shown in figures 3 and 4 for the 50 and 75 cm chord radii, respectively. As the figures show, there is excellent agreement between the finite element model of reference 6 and the analytical model of this study. Table 5 compares the simplified analytical solution of eqs. (52) and (61) for w_o to the finite element model results from reference 6 at the center of the solid spherical dome. The comparisons were excellent, with the worst-case difference being < 4 percent.

B. Perforated Shell Normal and Tangential Displacements

For the perforated material, only the 50 cm chord diameter was examined. Two aperture diameters were examined, and these were labeled screen and accelerator grid. The screen and accelerator grid aperture diameters were 0.899 and 0.399 cm, respectively, with an aperture center-to-center spacing of 0.953 cm for both. The same three materials as the prior section were examined. Effective material properties due to shell perforation under a plane stress load were determined from reference 14 and are listed in table 6. The grid thicknesses of table 2 were used. Geometric properties of the spherical domes are listed in table 3 for the 50 cm chord diameter. The constants used in the temperature equation are listed in table 4 for the 50 cm screen and accelerator grids. The equivalent finite element model results for the perforated grids were taken from Shunk, who modeled a spherical shell with apertures (ref. 6). Because of symmetry, Shunk modeled a perforated quarter section of the domed spherical grid using appropriate boundary conditions.

The normal displacements from the analytical and finite element models are shown in figures 5 and 6 for the screen and accelerator grids, respectively. Table 7 compares the simplified analytical solution of eqs. (52) and (61) for w_o to the finite element model results from reference 6 at the center of the perforated dome. As the figures and table show, there was good agreement between the analytical and finite element models for the titanium and molybdenum materials. The stainless steel material produced poorer comparisons, however.

Tangential displacements using the analytical model were determined for the perforated molybdenum and titanium grids. These tangential displacements are shown in figure 7 for both grids. Tangential displacements at the center and edge were both zero due to symmetry and setting $\Delta r_o = 0$, respectively.

C. Discussion of Results

For the solid shell results, normal displacement comparisons showed that the analytical model produced results that closely matched the finite element model of reference 6. This is not surprising because the assumptions used developing the above equations for thermally-induced shell displacements were the same as those commonly used for thin-walled shells of revolution (ref. 11). The simplified equation for the normal displacement of the spherical dome center was also found to accurately predict the displacement in this location, demonstrating that the simplified equation for w_o can be an accurate predictive tool.

Perforated shell normal displacement comparisons demonstrated that the use of effective material properties can produce inaccurate results in some cases, under-predicting the displacements at and near the grid center. It is speculated the discrepancies were likely the result of the steel's material properties and the use of effective material properties that can vary with load type. Reference 15 showed that a perforated plate with ratios of the material thickness divided by the center-to-center aperture spacing similar to all of those of this study should produce effective material properties that are a function of load type. It can be shown that the moments of eqs. (30) and (31) are directly proportional to

$$M_{\phi} \propto \frac{\alpha \cdot E \cdot h^3}{R} \propto M_{\theta}. \quad (66)$$

Because these moments produce bending loads, the steel screen grid would experience the highest bending loads because it had the highest thermal expansion coefficient, the second highest elastic modulus, and the highest thicknesses. As a result, the stainless steel produced poor comparisons to the finite element model.

The analytical model results for normal displacements still produced accurate results for the titanium and molybdenum materials, likely due to their lower thermal expansion coefficients. Table 7 shows that the simplified equation for w_0 yielded results that were within 3 percent of the results from the finite element model. Because most grid materials are either molybdenum or some other material with a low thermal expansion, this analytical approach should produce accurate results for these materials.

The analytical model results for tangential displacements showed that tangential displacements were significantly smaller than normal displacements. While it is likely the case that normal displacements will always be greater than tangential movement, the significantly small values in figure 7 were due, in part, to setting $\Delta r_0 = 0$. A larger value for Δr_0 would have caused larger tangential displacements.

From the aforementioned perforated plate results, changes in grid gap and grid-to-grid aperture alignment can be easily determined. At a given location r , grid gap and grid-to-grid aperture alignment changes are merely the difference of the normal and tangential displacements, respectively, of each grid.

VI. Conclusions

An analytical method for calculating the thermally-induced normal and tangential displacements of spherically domed grids was described. The theory for thin-walled shells of revolution under thermal loads varying both through the thickness and along surface was reviewed. Only spherical shells of uniform thickness and under an axisymmetric thermal loading were considered. A fixed edge support was used for this analysis. To make the analysis results more applicable, it was further assumed that the edge support could be thermally expanded.

Displacements both normal and tangential to the surface of the spherical shell were derived. A simplified equation for the displacement at the center of the spherical dome was also derived. This simplified expression for the displacement only requires knowledge of material properties, geometry of the spherical dome, temperatures at the center and edge, and the derivative of the temperature at the edge of the dome.

The effects of plate perforation on displacements and stresses were determined by modeling the perforated plate as an equivalent solid plate with modified, or effective, material properties. The effective material properties included the elastic modulus and Poisson's ratio. The resulting effective material properties are functions of the perforation pattern layout, aperture center-to-center spacing, and aperture diameter. The displacements in the actual perforated plate are the same as those of the equivalent solid plate utilizing effective material properties.

The analytical model was compared to the results from a finite element model for displacements normal to the surface. For the solid shell results, comparisons showed that the analytical model produced results that closely matched the finite element model results. The simplified equation for the normal displacement of the spherical dome center was also found to accurately predict the displacement in this location. For perforated shells, the analytical solution and simplified equation produced accurate results for the titanium and molybdenum materials, likely due to their lower thermal expansion coefficients. Because most grid materials are either molybdenum or some other material with a low thermal expansion, this analytical approach should produce accurate results for these materials.

The results from this study demonstrated that this analytical model can accurately predict grid displacements and can, therefore, be used as a predictive tool. The analytical equations presented in this study are further useful because they provide the relevant geometric and material parameters and their impact on grid displacements.

References

1. Diaz, E. and Soulas, G.C., "Hot Grid Gap Measurements of a NSTAR Thruster," IEPC Paper 2005-244, Oct.–Nov. 2005.
2. Soulas, G.C. and Frandina, M.F., "Ion Engine Grid Gap Measurements," AIAA Paper 2004-3961, July 2004.
3. Pollard, J.E. and Welle, R.P., "Thrust Vector Measurements with the T5 Ion Engine," AIAA Paper 95-2829, July 1995.
4. MacRae, G.S., Zavesky, R.J., and Gooder, S.T., "Structural and Thermal Response of 30 cm Diameter Ion Thruster Optics," AIAA Paper 89-2719, July 1989.
5. Ramsey, W.D., "12-cm Multi-Cusp Ion Thruster Inert Gas Performance," NASA Contractor Report CR-168208, Loral EOS Document 84-07-29, July 1984.
6. Shunk, D.D., "Finite Element Analysis of Ion Thruster Grids," M.S. Thesis, Department of Mechanical Engineering, Colorado State Univ., Fort Collins, CO, 2002.
7. MacRae, G.S. and Hering, G.T., "Status of Structural Analysis of 30 cm Diameter Ion Optics," AIAA Paper 90-2649, Jul. 1990.
8. Brophy, J.R. and Aston, G., "Thermal/Mechanical Analysis of Large Diameter ion Accelerator Systems," AIAA Paper 89-2718, Jul. 1989.
9. Nowacki, W., *Thermoelasticity*, Pergamon Presses Ltd., Oxford, 1962, pp. 505–514.
10. Johns, D.J., *Thermal Stress Analyses*, Pergamon Press, Oxford, 1965, pp. 88–96.
11. Timoshenko, S. and Woinowsky-Krieger, S., *Theory of Plates and Shells*, McGraw-Hill Book Company, Inc., New York, 1959, pp. 533–555.
12. Flugge, W., *Stresses in Shells*, Springer-Verlag, OHG., Berlin, 1960, pp. 312–344.
13. Abramowitz, M. and Stegun, I.A., *Handbook of Mathematical Functions with Formulas, Graphs, and Mathematical Tables*, Dover Publications, Inc., New York, 1970, pp. 332–335.
14. Slot, T. and O'Donnell, W.J., "Effective Elastic Constants for Thick Perforated Plates with Square and Triangular Penetration Patterns," *ASME Journal of Engineering for Industry*, vol. 11, no. 4, Nov. 1971, pp. 935–942.
15. O'Donnell, W.J. and Langer, B.F., "Design of Perforated Plates," *ASME Journal of Engineering for Industry*, vol. 841, no. 3, Aug. 1962, pp. 307–320.
16. Bailey, R. and Hicks, R., "Behaviour of Perforated Plates Under Plane Stress," *Journal of Mechanical Engineering Science*, vol. 2, no. 2, 1960, pp. 143–161.
17. Horvay, G., "The Plane-Stress Problem of Perforated Plates," *Journal of Applied Mechanics*, vol. 19, Sept. 1952, pp. 355–360.

TABLE 1.—SPHERICAL DOME MATERIAL
PROPERTIES AND THICKNESSES FROM REF. 6

Material	E, GPa	ν	α , m/m·°C
304 stainless steel	193	0.3	17.8×10^{-6}
Titanium	100	0.33	9.5×10^{-6}
Molybdenum	300	0.3	5.43×10^{-6}

TABLE 2.—SPHERICAL DOME THICKNESSES FROM REF. 6

Material	Screen h, cm	Accelerator h, cm
304 stainless steel	0.300	0.396
Titanium	0.152	0.203
Molybdenum	0.152	0.396

TABLE 3.—SPHERICAL DOME GEOMETRIES FROM REF. 6

Chord diameter	R, cm	ϕ_e
50 cm	85.75	16.95°
75 cm	128.62	16.95°

TABLE 4.—TEMPERATURE DISTRIBUTION CONSTANTS FROM REF. 6

Chord diameter and grid	A_{T0}	A_{T1}	A_{T2}
50 cm screen	-0.095	-0.636	283.3
50 cm accelerator	-0.096	-0.356	237.3
75 cm screen	-0.042	-0.423	283.4

TABLE 5.—COMPARISON OF SIMPLIFIED SOLUTION w_0 TO SOLID
SHELL FINITE ELEMENT MODEL RESULTS FROM REF. 6

Material	50 cm chord radius			75 cm chord radius		
	FEM, cm	Analytical, cm	Error, %	FEM, cm	Analytical, cm	Error, %
304 stainless steel	0.504	0.504	0.2	0.723	0.735	1.7
Titanium	0.259	0.258	-0.3	0.376	0.379	0.9
Molybdenum	0.145	0.147	1.6	0.210	0.216	3.2

TABLE 6.—PERFORATED SPHERICAL DOME EFFECTIVE MATERIAL PROPERTIES

Material	Screen grid		Accelerator grid	
	E, GPa	ν	E, GPa	ν
304 stainless steel	5.02	0.795	124	0.315
Titanium	2.60	0.795	64.1	0.334
Molybdenum	7.80	0.795	192	0.315

TABLE 7.—COMPARISON OF SIMPLIFIED SOLUTION w_0 TO PERFORATED
SHELL FINITE ELEMENT MODEL RESULTS FROM REF. 6

Material	Screen grid			Accelerator grid		
	FEM, cm	Analytical, cm	Error, %	FEM, cm	Analytical, cm	Error, %
304 stainless steel	0.655	0.573	-12.5	0.447	0.432	-3.47
Titanium	0.289	0.281	-2.77	0.221	0.219	-0.90
Molybdenum	0.165	0.161	-2.42	0.136	0.132	-2.94

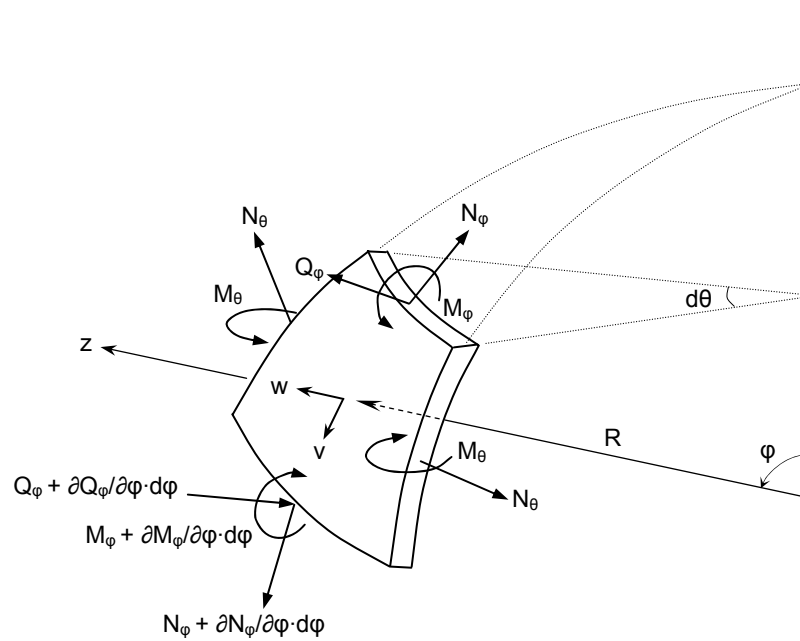


Figure 1.—Element of a spherical shell with the resultant forces and moments per unit length from an axisymmetric thermal load. Radius of curvature and resultant forces and moments are to the element middle surface.

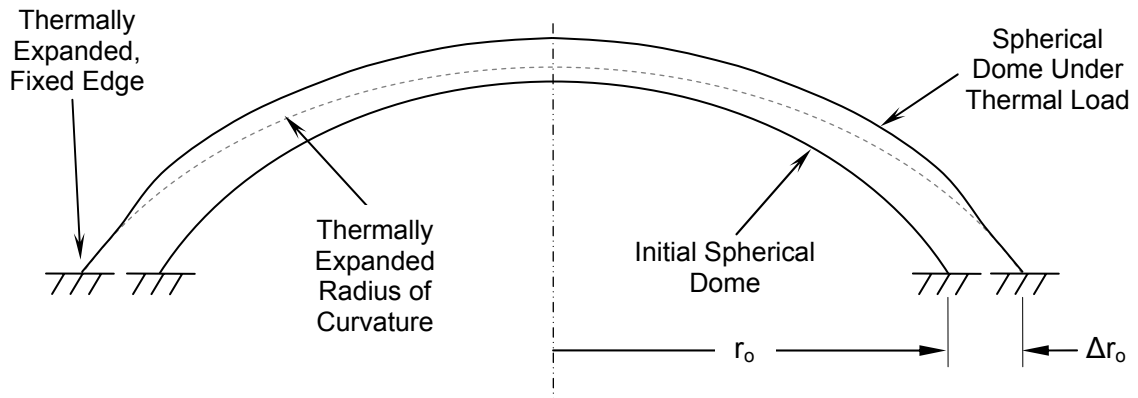


Figure 2.—Illustration of the boundary conditions used in this study for a spherically domed grid.

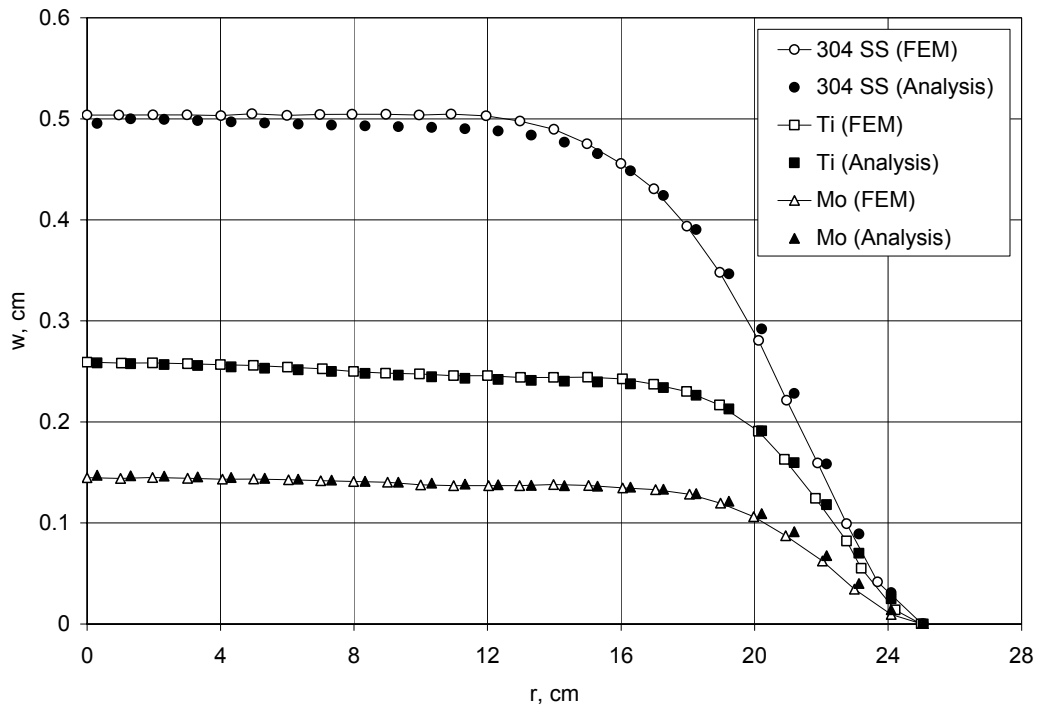


Figure 3.—Solid spherical dome displacements normal to the surface as a function of chord radius for the 50 cm chord diameter dome. Finite element model (FEM) results are from reference 6.

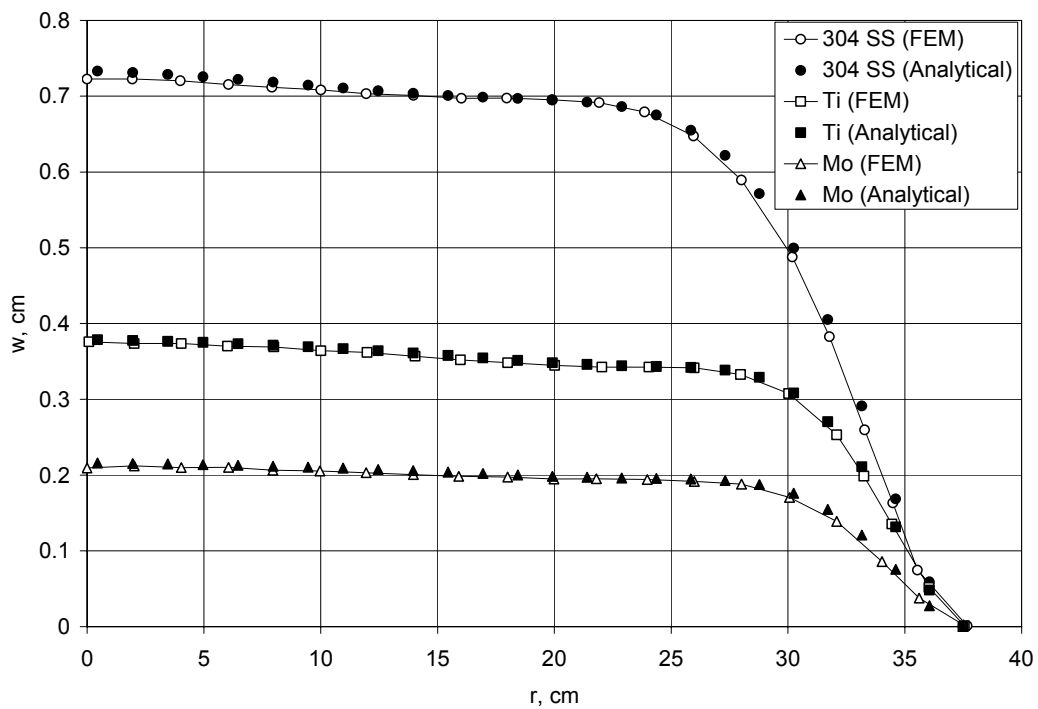


Figure 4.—Solid spherical dome displacements normal to the surface as a function of chord radius for the 75 cm chord diameter dome. Finite element model results are from reference 6.

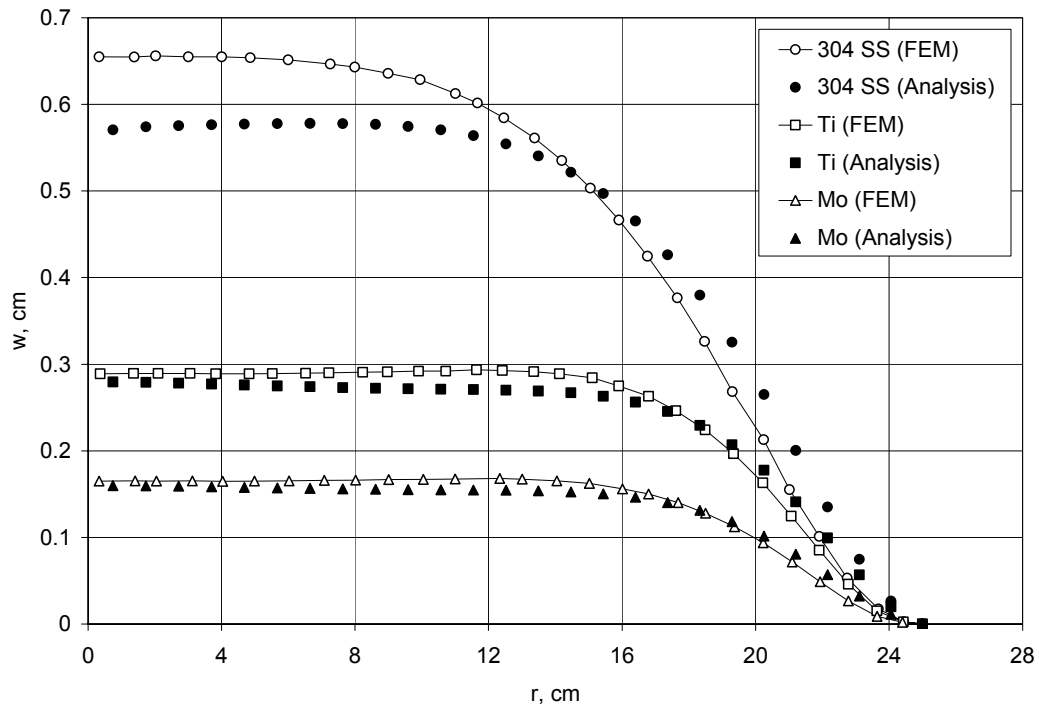


Figure 5.—Perforated spherical dome displacements normal to the surface as a function of chord radius for the 50 cm chord diameter screen grid. Finite element model results are from reference 6.

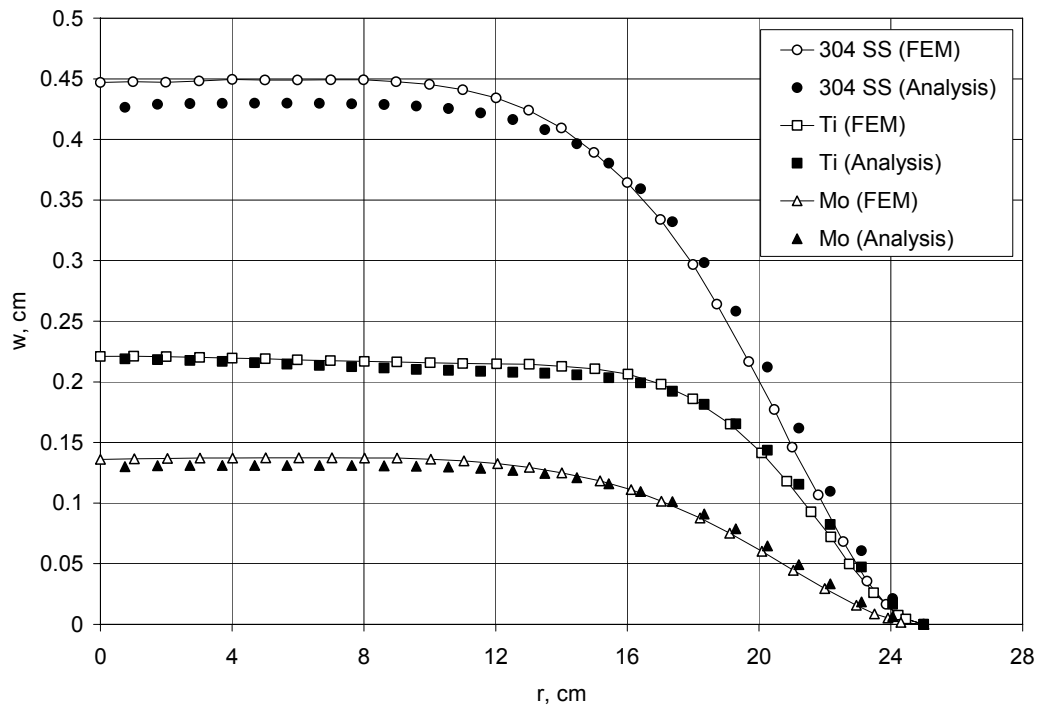


Figure 6.—Perforated spherical dome displacements normal to the surface as a function of chord radius for the 50 cm chord diameter accelerator grid. Finite element model results are from reference 6.

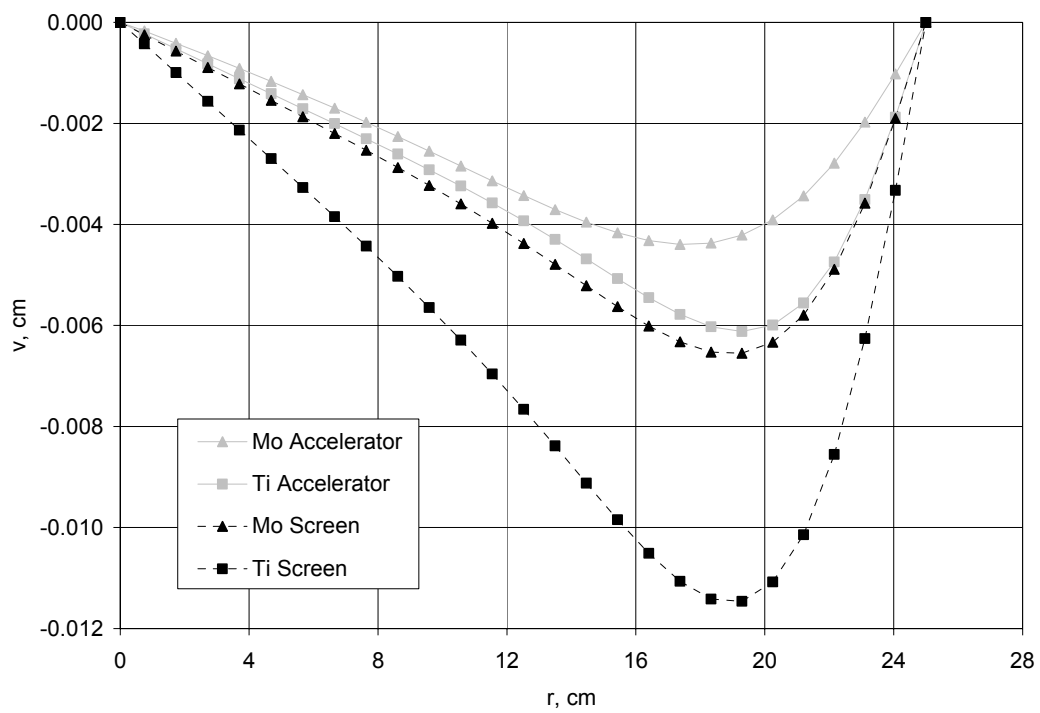


Figure 7.—Perforated spherical dome displacements tangential to the surface as a function of chord radius for the 50 cm chord diameter screen and accelerator grids.

REPORT DOCUMENTATION PAGE			Form Approved OMB No. 0704-0188	
Public reporting burden for this collection of information is estimated to average 1 hour per response, including the time for reviewing instructions, searching existing data sources, gathering and maintaining the data needed, and completing and reviewing the collection of information. Send comments regarding this burden estimate or any other aspect of this collection of information, including suggestions for reducing this burden, to Washington Headquarters Services, Directorate for Information Operations and Reports, 1215 Jefferson Davis Highway, Suite 1204, Arlington, VA 22202-4302, and to the Office of Management and Budget, Paperwork Reduction Project (0704-0188), Washington, DC 20503.				
1. AGENCY USE ONLY (Leave blank)		2. REPORT DATE March 2006		3. REPORT TYPE AND DATES COVERED Technical Memorandum
4. TITLE AND SUBTITLE Calculation of Thermally-Induced Displacements in Spherically Domed Ion Engine Grids			5. FUNDING NUMBERS WBS-22-612-50-04-19	
6. AUTHOR(S) George C. Soulas				
7. PERFORMING ORGANIZATION NAME(S) AND ADDRESS(ES) National Aeronautics and Space Administration John H. Glenn Research Center at Lewis Field Cleveland, Ohio 44135-3191			8. PERFORMING ORGANIZATION REPORT NUMBER E-15403	
9. SPONSORING/MONITORING AGENCY NAME(S) AND ADDRESS(ES) National Aeronautics and Space Administration Washington, DC 20546-0001			10. SPONSORING/MONITORING AGENCY REPORT NUMBER NASA TM-2006-214046 IEPC-2005-248	
11. SUPPLEMENTARY NOTES Prepared for the 29th International Electric Propulsion Conference cosponsored by ERPS, Princeton University, NASA Glenn, NASA Jet Propulsion Laboratory, Aerojet, EPPDYL, IEPC, Busek, and Mitsubishi Electric, Princeton, New Jersey, October 31-November 4, 2005. Responsible person, George C. Soulas, organization code RPP, 216-977-7419.				
12a. DISTRIBUTION/AVAILABILITY STATEMENT Unclassified - Unlimited Subject Categories: 20 and 37 Available electronically at http://gltrs.grc.nasa.gov This publication is available from the NASA Center for AeroSpace Information, 301-621-0390.			12b. DISTRIBUTION CODE	
13. ABSTRACT (Maximum 200 words) An analytical method for predicting the thermally-induced normal and tangential displacements of spherically domed ion optics grids under an axisymmetric thermal loading is presented. A fixed edge support that could be thermally expanded is used for this analysis. Equations for the displacements both normal and tangential to the surface of the spherical shell are derived. A simplified equation for the displacement at the center of the spherical dome is also derived. The effects of plate perforation on displacements and stresses are determined by modeling the perforated plate as an equivalent solid plate with modified, or effective, material properties. Analytical model results are compared to the results from a finite element model. For the solid shell, comparisons showed that the analytical model produces results that closely match the finite element model results. The simplified equation for the normal displacement of the spherical dome center is also found to accurately predict this displacement. For the perforated shells, the analytical solution and simplified equation produce accurate results for materials with low thermal expansion coefficients.				
14. SUBJECT TERMS Ion thruster; Ion engine; Ion propulsion; Mechanical engineering			15. NUMBER OF PAGES 26	
			16. PRICE CODE	
17. SECURITY CLASSIFICATION OF REPORT Unclassified	18. SECURITY CLASSIFICATION OF THIS PAGE Unclassified	19. SECURITY CLASSIFICATION OF ABSTRACT Unclassified	20. LIMITATION OF ABSTRACT	

